Investigation of glass-fibre reinforced polymers by polarisation-sensitive, ultra-high resolution optical coherence tomography: internal structures, defects and stress

Karin Wiesauer, Michael Pircher, Erich Götzinger, Christoph K. Hitzenberger, Reinhold Oster, David Stifter

Accepted Manuscript

Investigation of glass-fibre reinforced polymers by polarisation-sensitive, ultra-high resolution optical coherence tomography: internal structures, defects and stress

Karin Wiesauer, Michael Pircher, Erich Götzinger, Christoph K. Hitzenberger, Reinhold Oster, David Stifter

PII: S0266-3538(07)00175-3
DOI: 10.1016/j.compscitech.2007.04.018
Reference: CSTE 3676

To appear in: *Composites Science and Technology*

Received Date: 21 November 2006
Revised Date: 20 April 2007
Accepted Date: 25 April 2007

Please cite this article as: Wiesauer, K., Pircher, M., Götzinger, E., Hitzenberger, C.K., Oster, R., Stifter, D., Investigation of glass-fibre reinforced polymers by polarisation-sensitive, ultra-high resolution optical coherence tomography: internal structures, defects and stress, *Composites Science and Technology* (2007), doi: 10.1016/j.compscitech.2007.04.018

Investigation of glass-fibre reinforced polymers by polarisation-sensitive, ultra-high resolution optical coherence tomography: internal structures, defects and stress

Karin Wiesauer[1,*], Michael Pircher[2], Erich Götzinger[2], Christoph K. Hitzenberger[2], Reinhold Oster[3], David Stifter[1]

[1]Upper Austrian Research GmbH, Hafenstr. 47-51, 4020 Linz, Austria

[2]Center for Biomedical Engineering and Physics, Medical University of Vienna, Währingerstr. 13, 1090 Wien, Austria

[3]Eurocopter Deutschland GmbH, 81663 München, Germany

[*]Corresponding author. Tel.: + 43 732 90 1556 06; fax: + 43 732 90 1556 18.

E-mail address: karin.wiesauer@uar.at (K. Wiesauer).

Abstract

In this paper, we report on optical coherence tomography (OCT) for the investigation of glass-fibre reinforced polymer (GFRP) materials. OCT, a contactless and non-destructive imaging technique, provides depth-resolved information on internal structures within semi-transparent materials. In our study, we apply a highly advanced OCT technique: we use transversal scanning, ultra-high resolution, polarisation-sensitive (UHR-PS-)OCT for the analysis of various GFRP samples. UHR-imaging with resolution in the micron range is shown to provide information on the scale of single fibres. PS-OCT, an extension of classical OCT, is sensitive to birefringence and consequently to anisotropies and stress within a material. Our system is therefore applied to the investigation of defects located within the fibre layers of loaded and damaged GFRP samples. Imaging of matrix fracture, cracks, and internal stress, demonstrates the high potential of UHR-PS-OCT for the investigation of damage in GFRP materials, with special emphasis on detecting the early stages of defect formation.

Keywords: Glass fibres A, polymer-matrix composites A, defects B, residual stress C, non-destructive testing D.

1. Introduction

Due to their lower weights when compared to metal structures, fibre reinforced polymer materials are widely used in many areas including aviation, aeronautics and automotive engineering. Because of high demands on mechanical performance, the investigation of the structural integrity of these materials, especially when subjected to impact, has become a crucial issue in current research. Techniques such as ultrasonics (with developments in air-coupled and laser ultrasonics) [1,2], active thermography (optically or ultrasonically excited) [3], shearography [4], or electronic speckle pattern interferometry (ESPI) [5] are commonly applied for non-destructive testing (NDT) of these structures and their defects, each with its specific strengths and limitations. However, none of these methods allows imaging of the structures on the scale of single fibres.

A technique demonstrated to be capable of depth-resolved imaging of glass-fibre reinforced polymer (GFRP) materials on the micron scale is optical coherence tomography (OCT) [6-8]: OCT is a non-destructive and contactless method for high-resolution imaging of internal structures within semi-transparent media [9]. Originally developed for biomedical applications, it has only recently attracted interest in the materials sector, with various kinds of applications ranging from e.g., imaging of subsurface cracks in ceramics, Teflon or SiC [10,11], the investigation of injection moulded plastic parts, thin multi-layer foils and coatings [8,12], to the analysis of the subsurface morphology of archaic jades [13]. In the field of fibre composites, OCT is well suited for the investigation of semi-transparent materials such as GFRP [6-8]. However, composites containing conducting fibres (e.g. carbon fibres) or metal composites are not suitable for OCT imaging because of their opacity. In addition to the classical OCT technique, different modifications exist, among these transversal OCT [14], ultra-high resolution (UHR-)OCT [15], and polarisation-sensitive OCT (PS-OCT), with PS-OCT providing additional contrast using birefringence [16,17].

In this paper, we report on the application of a highly advanced OCT technique combining the three above listed modifications, namely transversal scanning UHR-PS-OCT for the investigation of GFRP

materials. First, the special requirements for OCT when used for imaging of fibre structures are discussed. Second, we apply our transversal UHR-PS-OCT system to study defects within damaged and externally loaded samples: by investigating matrix fracture, cracks and internal stress, the potential of this technique for structural analysis of GFRP materials is demonstrated.

2. OCT principles and experimental setup

OCT is based on the principles of white-light interferometry, using broadband light sources in the near-infrared (NIR). In general, an OCT system consists of an interferometer where the incident light is split into one part illuminating the sample and another part which is reflected by a reference mirror (see fig. 1(a)). The light illuminating the sample is back-scattered and reflected by internal structures located at different depths within the sample. Sample and reference beams are re-combined and the interference signal is recorded by a detector.

One particular property of broadband light used for OCT imaging is its very short coherence length. The coherence length gives the distance of wavefront propagation within which the amplitude and phase of the wave can be considered well defined. Therefore, interference can only be observed if the optical path lengths of the interfering rays do not differ for more than the coherence length. In contrast to conventional narrowband laser radiation with coherence lengths in the range of meters, the coherence length of broadband light sources used for OCT imaging can range down to only a few microns. Therefore, in an OCT setup, the scattering or reflecting internal structures at different depths of the sample can be detected by moving the reference mirror. One depth-scan of the reference mirror provides a depth-resolved reflectivity profile of the sample (see fig. 1(b)), with the depth-resolution Δz mainly determined by the coherence length of the light source [18]:

$$\Delta z = \frac{2\ln(2)}{\pi} \cdot \frac{\lambda_c^2}{\Delta\lambda}, \qquad (1)$$

where λ_c is the centre wavelength and $\Delta\lambda$ the bandwidth of the light source. For commonly used broadband light sources such as superluminescence diodes (SLDs), a depth resolution of 10-20 µm is provided. Using

special light sources, for example femtosecond (fs-)lasers, depth-resolutions down to about 1 μm can be reached [15]. The lateral resolution is independently determined by the optics focusing the probing beam on the sample. In general, cross-sectional images are obtained by laterally shifting the laser beam with respect to the sample and by combining the subsequent depth-scans.

In OCT imaging, the penetration depth strongly depends on the sample properties. For materials semi-transparent in the NIR, e.g. many plastics and polymers, penetration depths up to several millimetres can be achieved. In general, lower penetration depths for light sources with shorter wavelengths can be expected due to enhanced scattering (for instance, when comparing a Ti:sapphire fs-laser with a centre wavelength λ_c = 800 nm to SLDs operating in the telecommunication band around 1550 nm). However, ultra-high resolution OCT imaging has commonly been achieved for the shorter wavelengths.

In this work, we have combined concepts of transversal scanning OCT developed by Hitzenberger *et al.* [19] and refined by Pircher *et al.* for PS-OCT [20,21] with the benefits of UHR imaging, as described in detail in ref. [12]. Furthermore, we have extended this transversal UHR-OCT setup for polarisation-sensitive measurements [22]. The resulting transversal UHR-PS-OCT system schematically shown in fig. 2 is based on a Mach-Zehnder interferometer geometry (a detailed description of the setup can be found in ref. [22]). The light source, a Ti:sapphire fs-laser operating at λ_c = 800 nm, provides a depth-resolution of 2.45 μm in air, corresponding to a depth-resolution of 1.63 μm in material (assuming a refractive index of 1.5, an approximate value common for many epoxy resins). In combination with a lateral resolution of 4 μm, UHR imaging is obtained. Transversal (or en-face) scanning, in contrast to conventional cross-sectional imaging, provides in-plane information parallel to the sample surface, which is of interest for many problems posed in materials research [12]. In our setup, transversal scanning is obtained by the use of an *xy*-galvano scanner unit which raster-scans the laser beam over the sample in two directions while the position of the reference mirror is kept fixed, corresponding to the measurement at a defined optical depth within the sample. Heterodyne signal detection is applied using two acousto-optic modulators (AOMs) for a signal modulation frequency of 2 MHz, and dual balanced detection results in an enhanced signal to noise ratio. As alternative to transversal scanning, cross-sectional imaging can be performed by repeatedly scanning the laser beam along a line across

the sample while one depth-scan of the reference mirror is performed. Transversal scan areas up to 5x5 mm^2 can be measured, with an acquisition time of e.g. 8 seconds for $4*10^6$ data points (2 µs/pixel).

For polarisation-sensitive measurements, quarter-wave plates (QWPs) were added in the two interferometer arms, producing circularly polarised light irradiating the sample, and linearly polarised light oriented 45° with respect to the horizontal in the reference arm. Any birefringence within the sample changes the circular polarisation into a generally elliptical one. The state of polarisation of the interference signal is measured by polarisation-sensitive detection units comprised of polarising beam splitters (PBSs) that separate the light into two orthogonal polarisation components before detection. From the signals of the two detection channels, three types of images can be obtained simultaneously [23]: *i)* the conventional reflectivity image, *ii)* the retardation between the signals and *iii)* the orientation of the optical axis can be calculated. The retardation provides depth-resolved information about internal birefringence Δn [24], with $\Delta n = (n_{\parallel} - n_{\perp})$ determined by the difference between the refractive indices $n_{\parallel}$ and $n_{\perp}$ of the two orthogonal polarisation components of the interference signal, a value related to anisotropies and stress within the sample. On the other hand, the orientation of the optical axis is indicative of the direction of the stress fields and anisotropies [22].

3. OCT-imaging of GFRP materials

When OCT is applied to the investigation of GFRP materials, systems providing a standard depth-resolution of 10-20 µm are in general not useful for imaging on the scale of individual fibres with diameters typically in the range of only a few microns. Consequently, ultra-high resolution imaging is needed. For illustration, we have investigated a GFRP sample using two different light-sources. The specimen was a pre-impregnated (pre-preg) composite fibre sheet consisting of perpendicularly woven fibre bundles with fibre diameters of around 9 µm. A SLD providing a depth-resolution of 19 µm in air and the fs-laser described above were used as sources, with the corresponding cross-sectional images displayed in figs. 3(a) and (b). In the SLD image (obtained with a different OCT setup described in ref. [8]), the optical thickness of the sheet of about 300 µm is revealed, corresponding to a geometrical layer thickness of 200 µm when a refractive index of 1.5 is

assumed. However, the internal structure with the fibre bundles is only coarsely visible. In contrast, the UHR image in fig. 3(b) clearly shows the parallel and perpendicular fibre bundles with the single fibres resolved. The dark spots (as indicated by the arrow in fig. 3(b)) correspond to air pores within the bundles.

By transversal imaging, in-plane information at a defined optical depth is obtained. The UHR-en-face image displayed in fig. 3(c), recorded at an optical depth indicated by the dotted line in (b), clearly reveals the lateral arrangement of the woven fibre bundles within the sample. Transversal scanning provides this depth-resolved in-plane information within only one measurement. This is in contrast to common cross-sectional OCT systems where in-plane information can only be obtained by acquiring a full 3D dataset consisting of a series of cross-sectional scans and by subsequent extraction of the in-plane information via time-consuming software procedures.

Nevertheless, the acquisition and analysis of full 3D datasets can be useful to obtain information about the entire spacial arrangement of internal structures, as is demonstrated in the following. We have acquired 3D datasets of different knitted GFRP samples by recording transversal scans at successive optical depths. The composite material reinforced with weft-knit fabric is made of commingled yarn fabrics composed of glass- and thermoplastic fibres [25] and is processed under elevated temperature and pressure. The 3D renderings displayed in fig. 4(a-c) show the upper 300 µm of the samples, each consisting of en-face scans recorded at depth intervals of 20 µm, revealing the spacial arrangements of the fibre loops.

4. Investigation of defects and stress by UHR-PS-OCT

When GFRP materials are subjected to external loading, internal stress fields give rise to structural defects once a critical value is exceeded. Therefore, the analysis of internal stresses is an issue of interest for the investigation of failure of GFRP materials. We have applied UHR-PS-OCT imaging for the analysis of externally strained samples, and for samples bearing defects due to prior loading tests. By these measurements, information about internal structure and stress was simultaneously obtained. PS-OCT for imaging of GFRP samples has already been performed [26]. However, this setup was incapable of resolving

individual fibres. In this work, we demonstrate for the first time UHR-PS-OCT imaging of GFRP samples, providing both, imaging of single fibres and mapping of internal stress on the micron range.

The investigation of structural failure and mapping of the corresponding internal stress were performed on a 2 mm thick GFRP laminate consisting of woven layers of perpendicularly arranged rovings within an epoxy resin matrix. The sample was fixed at two opposite edges and was externally loaded by applying a force to the centre part from the rear side, resulting in a bending of the sample. Figures 5(a)-(h) show the cross-sectional reflectivity and corresponding retardation images of the increasingly stressed sample. In the reflectivity images the fibre layers with their single fibres are resolved, as is illustrated by the inset in (c) where a magnified view of a fibre bundle is given. In the retardation images, the retardation values between the two orthogonal polarisation components are displayed colour-coded from 0° (blue) to 90° (red). If the sample is non-birefringent, no phase retardation is observed (0°, blue). A value of 90° (red) corresponds to a phase lag of a quarter wavelength between the two orthogonal polarisation directions due to birefringence. It is noted that the retardation is only defined for signal values above the noise level [20], i.e. where backscattering structures are present within the sample. Consequently, in regions with intensity values below a certain threshold the retardation is displayed in grey (intensity filtered).

In figs. 5(a) and (b) the reflectivity and retardation images of the sample prior to loading are displayed. No retardation is found for the unstrained GFRP sample, indicating that no residual stresses and anisotropies are present. Figures 5(c)-(f) show the intensity and corresponding retardation images when loading of the GFRP specimen was successively increased. Initially, no structural change of the fibre composite takes place (c), but in the retardation image (d) the appearance of birefringence, i.e. of internal stress is observed (yellow-red colour values of the fibre bundles). When bending is increased, matrix fracture sets in. The arrows in (e) indicate an area where such structural damage of the composite has emerged below the first fibre layer. Again, the internal stress is mapped by the retardation image (f). Subsequently, the sample was released, with a small amount of residual stress remaining, as is evidenced by the bluish-green colour values of the fibre bundles (h). However, the defects are still clearly visible (g), showing that irreversible structural damage has occurred. The apparent lateral displacement of the fractured areas in (g) with respect to

(e) results from imaging at slightly different positions because of sample movement during bending and releasing.

An effect which could disturb the observation of birefringence in scattering media is depolarisation. Depolarisation is caused by multiple scattering events within the sample [27], resulting in a loss of polarisation of the probing beam. Therefore, arbitrary values of the retardation and the orientation of the optical axis would be detected. However, within the penetration depth of our fibre samples no noticeable depolarisation was observed, as is evidenced e.g. in fig. 5(b) where the colouring of the fibre bundles remains at a constant blue value over the whole observation depth.

In fig. 6 the damaged sample presented above is shown in a more magnified view. The cross-sectional UHR-OCT image in (a) was recorded across an extended, strongly scattering defect, where the topmost woven fibre layer has been delaminated from the underlying material. For comparison, a polished micrograph section of the sample was taken with an optical microscope in the vicinity of the site measured by OCT. The obtained micrograph (fig. 6(b)) confirms the presence and location of the matrix fracture below the first woven fibre layer. Additionally, in both images the perpendicularly arranged fibre bundles (indicated by the dashed lines) and the single fibres are visible.

As a final example for defect analysis by PS-OCT, the outer skin of a helicopter rotor blade was investigated. The rotor blade was composed of a closed porous core and a GFRP laminate skin. The matrix material of the GFRP was a thermosetting epoxy resin; the fibre rovings arranged along two directions consisted of fibres with diameters of about 9-10 µm. The rotor blade was subjected to loading tests by shear force free bend, resulting in the formation of cracks within the aerodynamic region of the rotor blade profile.

In fig. 7(a), a cross-sectional OCT scan of a crack-free part of the skin is shown. The marked area indicates a fibre bundle of the first fibre sheet layer, located at an optical depth of around 350 µm below the epoxy surface (corresponding to a geometrical depth of around 230 µm for a refractive index of 1.5). When scanning across a crack, the crack itself is hardly visible (upper arrow in fig. 7(b)) because it is more or less

parallel to the incident laser beam and therefore generates nearly no back-reflection. However, in combination with the crack a strongly scattering extended defect (marked by the two arrows) located at the uppermost fibre layer was detected. The corresponding retardation image in fig. 7(c) reveals that enhanced birefringence is present in the fibre bundles close to the crack. Interestingly, this effect has not been observed for the damaged and unloaded sample shown in fig. 5(h), where the first fibre layer was located close to the surface, in contrast to the sample in fig. 7.

A clearer view of the crack is obtained by transversal scanning. For crack-free regions, the en-face reflectivity image recorded at an optical depth of the first fibre layer shows the woven rovings of the fibre sheet (fig. 8(a)), and the retardation image indicates that no birefringence is present (fig. 8(b)). Additionally, the orientation of the optical axis was determined (e.g. in fig. 8(c) for the undamaged region) which, just as the retardation, was calculated only for signal values above a certain intensity threshold. Also for the case of strictly zero birefringence, the orientation of the optical axis is not defined [23]. The orientation of the optical axis is colour-coded from 0° (red), over 90° (turquoise), to 180° (red) equivalent to 0° in the images. When a transversal scan over a straight crack at an optical depth as indicated by the dotted line in fig. 7(b) is performed, the crack running vertically across the fibres becomes visible in the reflectivity image (arrows in fig. 8(d)), and at the laminar defect enhanced back-scattering is observed. In the corresponding retardation image, increased birefringence is present in the fibre-reinforcement close to the crack, clearly marking the crack position (fig. 8(e)). The orientation of the optical axis influences a wide area on both sides of the crack and not only where the defect is present, with a value of around 0° (mainly red colour values) at the crack indicating an optical axis and thus either stress fields or anisotropies perpendicular to the crack. In general, when comparing the images without and with crack, the retardation and the optical axis images reveal at a glance whether a crack is present (in contrast to the reflectivity image), in that way providing an enhanced contrast mechanism for crack detection.

5. Discussion and conclusions

In this work we, have applied for the first time transversal scanning UHR-PS-OCT for non-destructive and contactless analysis of GFRP materials. By comparison with standard OCT-imaging, it is shown that UHR-

OCT is an essential condition for structural investigations of these materials due to the small feature sizes of the fibre structures. Additionally, the benefits of a transversal scanning OCT system are demonstrated, directly providing in-plane information which cannot be easily accessed by conventional cross-sectional OCT imaging.

Particular attention was paid to the detection of defects. OCT imaging of defects in GFRP materials has been demonstrated before [7], but so far only with standard resolution, in contrast to the present work where UHR-OCT imaging is applied. Especially with regard to the initiation of failure of components, enhanced resolution can provide insight into the very early stages of structural damage and can reveal failure parameters with increased precision. UHR-OCT has the capability of resolving backscattering structures and defects with lateral sizes of only a few microns, as e.g. exemplified in the reflectivity images in fig. 5. This accuracy is obtained by none of the standard NTD methods commonly used for defect detection, such as ultrasonics, active thermography or shearography. A technique providing resolution comparable or even superior to UHR-OCT is confocal microscopy since it is used in a variety of applications for biomedical imaging. However, its application is limited to relatively transparent materials and near-surface regions because image contrast is strongly degraded in scattering media [28]. A direct comparison between confocal microscopy and OCT has shown an increased signal to noise ratio and an up to three times higher penetration depth for OCT [28]. A recent study where both techniques have been applied for characterisation of defects in GFRP materials also confirmed that by OCT the samples could be probed deeper and with more image detail [7].

We also have applied UHR-PS-OCT for the investigation of structural failure in an externally strained GFRP sample. By comparison with optical microscopy, it was proven that defects formed during loading could be clearly identified by the OCT measurements. Furthermore, it was shown that UHR-PS-OCT is capable of imaging the damage process while simultaneously mapping the internal stress state. So far, only arbitrary strain values have been applied to the sample. However, UHR-PS-OCT can reveal critical parameters such as the stress values where structural damage initiates in future experiments using defined

loading conditions similar to ref. [24]. Another issue of interest was the investigation of cracks in the GFRP skin of helicopter rotor blades by transversal UHR-PS-OCT. These experiments revealed a correlation between cracks, birefringence and orientation of the optical axis, providing an additional contrast mechanism for crack detection.

With these applications, we clearly demonstrate the high potential of UHR-PS-OCT for the investigation of GFRP materials. The unique combination of its non-destructive and contactless character with the ability of depth-resolved ultra-high resolution imaging makes UHR-PS-OCT a promising tool for further characterisation of internal structures, defects and stress within GFRPs.

Acknowledgments

This work has been supported by the Austrian Science Fund FWF (Projects: P16585-N08 and L126-N08). Furthermore, we would like to thank Karin Thielsch and Georg Haasemann from the Institut für Festkörpermechanik, TU Dresden (Germany) for kindly providing the knitted GFRP samples, which have been fabricated within the context of the priority program (SPP) no. 1123 and the collaborative research centre (SFB) no. 639 funded by the German Research Community (DFG).

References

1. Stoessel R, Krohn N, Pfleiderer K, Busse G. Air-coupled ultrasound inspection of various materials. Ultrasonics 2002;40(1-8):159-163.

2. Monchalin JP, Neron C, Bouchard P, Choquet M, Heon R, Padioleau C. Inspection of composite materials by laser-ultrasonics. Canadian Aeronautics and Space Journal 1997;43(1):34-38.

3. Ghosh KK, Karbhari VM. A critical review of infrared thermography as a method for non-destructive evaluation of FRP rehabilitated structures. Int J Materials and Product Technology 2006;25(4):241-266.

4. Newman JW. Shearographic inspection of aircraft structure. Materials Evaluation 1991;49(9):1106-1109.

5. Wang WC, Day CH, Hwang CH, Chiou TB. Nondestructive evaluation of composite materials by ESPI. Research in Nondestructive Evaluation 1998;10(1):1-15.

6. Dunkers JP, Parnas RS, Zimba CG, Peterson RC, Flynn KM, Fujimoto JG, Bouma BE. Optical coherence tomography of glass reinforced polymer composites. Composites A 1999;30(2):139–145.

7. Dunkers JP, Phelan FR, Sanders DP, Everett MJ, Green WH, Hunston DL, Parnas RS. The application of optical coherence tomography to problems in polymer matrix composites. Opt Laser Eng 2001;35(3):135-147.

8. Stifter D, Burgholzer P, Höglinger O, Götzinger E, Hitzenberger CK. Polarisation-sensitive optical coherence tomography for material characterisation and strain-field mapping. Appl Phys A 2003;76(6):947-951.

9. Huang D, Swanson EA, Lin CP, Schuman JS, Stinson WG, Chang W, Hee MR, Flotte T, Gregory K, Puliafito CA, Fujimoto JG. Optical Coherence Tomography. Science 1991;254(5035):1178-1181.

10. Bashkansky M, Duncan MD, Kahn M, Lewis III D, Reintjes J. Subsurface defect detection in ceramics by high-speed high-resolution optical coherent tomography. Opt Lett 1997;22(1):61-63.

11. Duncan MD, Bashkansky M, Reintjes J. Subsurface defect detection in materials using optical coherence tomography. Opt Express 1998;2(13):540-545.

12. Wiesauer K, Pircher M, Götzinger E, Bauer S, Engelke R, Ahrens G, Grützner G, Hitzenberger CK, Stifter D. En-face scanning optical coherence tomography with ultra-high resolution for material investigation. Opt Express 2005;13(3):1015-1024.

13. Yang ML, Lu CW, Hsu IJ, Yang CC. The use of Optical Coherence Tomography for Monitoring the Subsurface Morphologies of Archaic Jades. Archaeometry 2004;46(2):171-182.

14. Podoleanu AG, Dobre GM, Jackson DA. En-face coherence imaging using galvanometer scanner modulation. Opt Lett 1998;23(3):147-149.

15. Drexler W, Morgner U, Kärntner FX, Pitris C, Boppart SA, Li XD, Ippen EP, Fujimoto JG. In vivo ultrahigh-resolution optical coherence tomography. Opt Lett 1999;24(17):1221-1223.

16. Hee MR, Huang D, Swanson EA, Fujimoto JG. Polarisation-sensitive low-coherence reflectometer for birefringence characterisation and ranging. J Opt Soc Am B 1992;9(6):903-908.

17. de Boer JF, Milner TE, van Gemert MJC, Nelson JS. Two-dimensional birefringence imaging in biological tissue by polarisation sensitive optical coherence tomography. Opt Lett 1997;22(12):934-936.

18. Swanson EA, Huang D, Hee MR, Fujimoto JG, Lin CP, Puliafito CA. High-speed optical coherence domain reflectometry. Opt Lett 1992;17(2):151-153.

19. Hitzenberger CK, Trost P, Lo PW, Zhou Q. Three dimensional imaging of the human retina by high-speed optical coherence tomography. Opt Express 2003;11(21):2753-2761.

20. Pircher M, Goetzinger E, Leitgeb R, Hitzenberger CK. Transversal phase resolved polarisation sensitive optical coherence tomography. Phys Med Biol 2004;49(7):1257-1263.

21. Pircher M, Goetzinger E, Leitgeb RA, Sattmann H, Hitzenberger CK. Ultrahigh resolution polarisation sensitive optical coherence tomography. Coherence Domain Optical Methods and Optical Coherence Tomography in Biomedicine IX, Proc of SPIE 2005;5690:257-262.

22. Wiesauer K, Pircher M, Götzinger E, Hitzenberger CK, Engelke R, Ahrens G, Grützner G, Stifter D. Transversal ultrahigh-resolution polarisation sensitive optical coherence tomography for strain mapping in materials. Opt Express 2006;14(13):5945-5953.

23. Hitzenberger C, Götzinger E, Sticker M, Pircher M, Fercher AF. Measurement and imaging of birefringence and optic axis orientation by phase resolved polarisation sensitive optical coherence tomography. Opt Express 2001;9(13):780-790.

24. Wiesauer K, Sanchis Dufau AD, Götzinger E, Pircher M, Hitzenberger CK, Stifter D. Non-destructive quantification of internal stress in polymer materials by polarisation sensitive optical coherence tomography. Acta Materialia 2005;53(9):2785-2791.

25. Haasemann G, Kästner M, Ulbricht V. Multi-scale modelling and simulation of textile reinforced materials. Computers Materials & Continua 2006;3:131-146.

26. Oh JT, Kim SW. Polarization-sensitive optical coherence tomography for photoelasticity testing of glass/epoxy composites. Opt Express 2003;11(14):1669-1676.

27. Zimnyakov DA. Light correlation and polarization in multiply scattering media: industrial and biomedical applications. In: Tuchin VV, editors. Handbook of coherent domain optical methods: biomedical diagnostics, environmental and material science, vol. 1. Boston/Dodrecht/London: Kluwer Academic Publishers, 2004.

28. Izatt JA, Hee MR, Owen GM. Optical coherence microscopy in scattering media. Opt Lett 1994;19(8):590-592.

Figure Captions

Figure 1:

(a) Schematic drawing of a standard OCT setup and (b) typical interference signal of a layered, semitransparent sample obtained by one depth-scan of the reference mirror. A: distance beam splitter – sample surface, B: layer thickness, n: refractive index of the sample.

Figure 2.

Schematic drawing of the UHR-PS-OCT setup with a fs-laser as light source. The respective polarisation states of the laser beam are indicated by the bold arrows. Abbreviations: AOM – acousto-optic modulator, (N)PBS – (non-)polarising beam splitter, QWP – quarter-wave plate, SMF – single-mode fibre, DAQ – data-acquisition.

Figure 3.

OCT images of a GFRP sheet. Cross-sectional scans obtained with (a) a SLD (depth-resolution 19 µm in air) and (b) a fs-laser (depth-resolution 2.45 µm in air) as light sources. The arrow marks an air pore within a bundle. (c) UHR-en-face scan at an optical depth indicated by the dotted line in (b).

Figure 4.

3D renderings obtained from stacks of subsequent en-face scans for different kinds of knitted GFRP fabrics (scan areas: (a),(b): 5x5 mm^2, (c): 3x3 mm^2; displayed depths: 300 µm).

Figure 5.

Cross-sectional UHR-PS-OCT images of a GFRP sample. (a), (c), (e) and (g): reflectivity images, (b), (d), (f) and (h): corresponding retardation images (retardation colour-coded from 0° to 90°). (a), (b): unloaded sample. (c-f): sample increasingly bent. (g), (h): released sample. The inset in (c) shows a magnified view of a fibre bundle. In (e), an area where matrix fracture has taken place is marked by the arrows. All images were recorded at slightly different positions on the sample.

Figure 6.

(a) OCT cross-sectional image and (b) polished micrograph section, both showing matrix fracture below the first fibre sheet (the dashed lines indicate parallel and perpendicular fibre bundles).

Figure 7.

Cross-sectional UHR-PS-OCT scans of the GFRP skin of a helicopter rotor blade. (a) Crack-free area with an individual fibre bundle marked. (b) Scan across a crack (indicated by the upper arrow). In combination with the crack, a defect at the uppermost fibre layer is observed, as marked by the two arrows. (c) Corresponding retardation image (retardation colour-coded from 0° to 90°). The area around the roving below the crack shows increased birefringence.

Figure 8.

En-face UHR-PS-OCT scans of the GFRP skin of a helicopter rotor blade. (a) and (d): reflectivity, (b) and (e): retardation (colour-coded from 0° to 90°), (c) and (f): orientation of the optical axis (colour-coded from 0° to 180°). (a)-(c): crack-free region. (d)-(f): scan across a crack marked by the arrows. Close to the crack, birefringence and a change in the orientation of the optical axis are observed.

Figure 1:

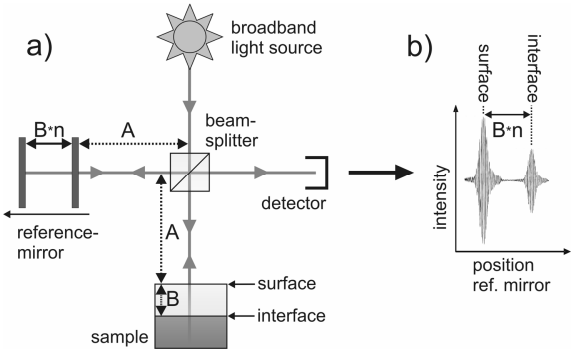

Figure 2 (two columns suggested):

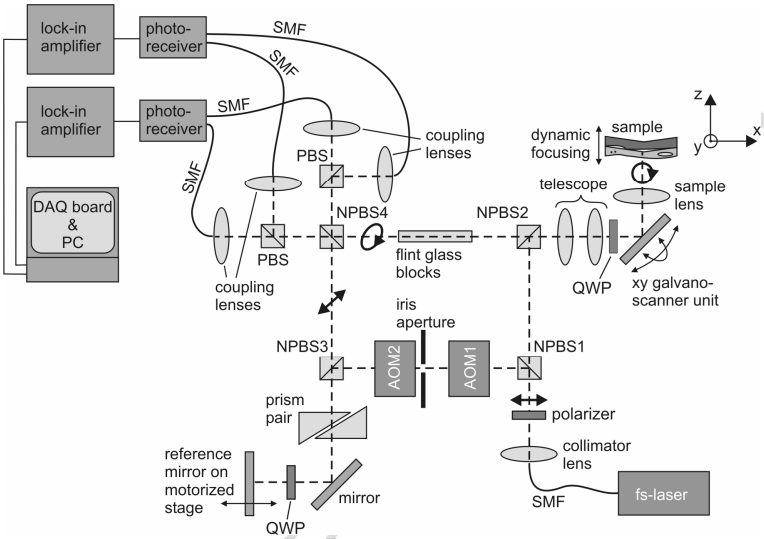

Figure 3 (two columns suggested):

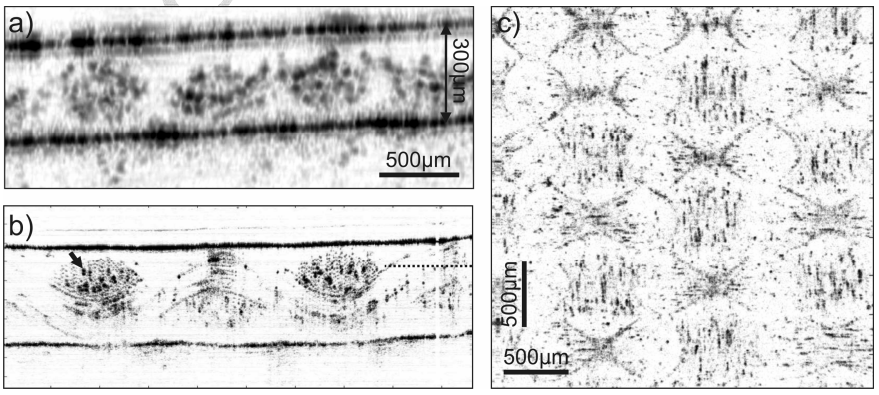

Figure 4 (two columns suggested):

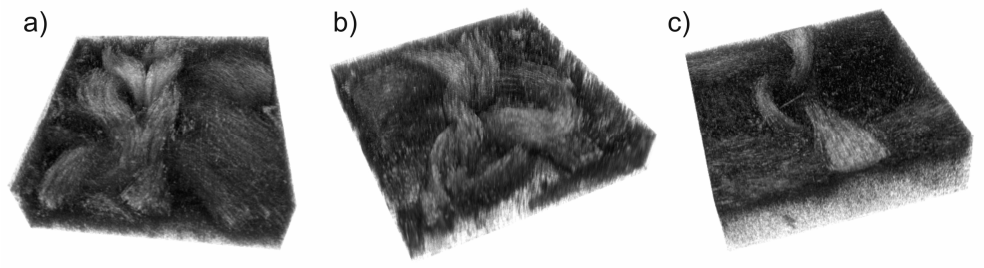

Figure 5 (two columns suggested):

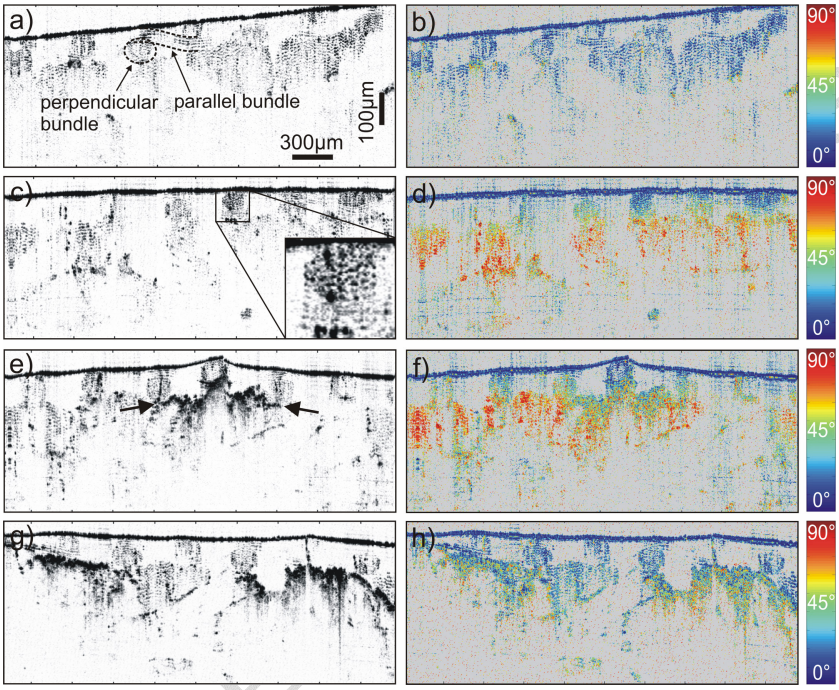

Figure 6:

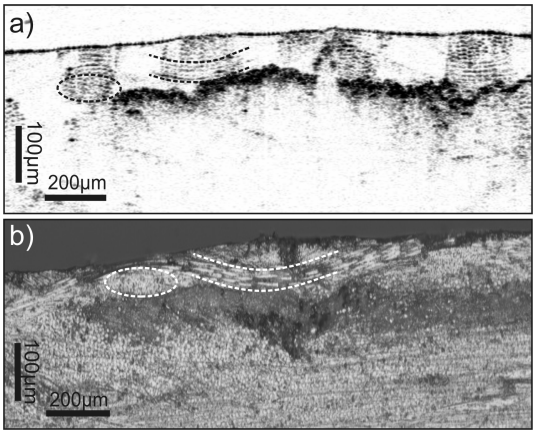

Figure 7:

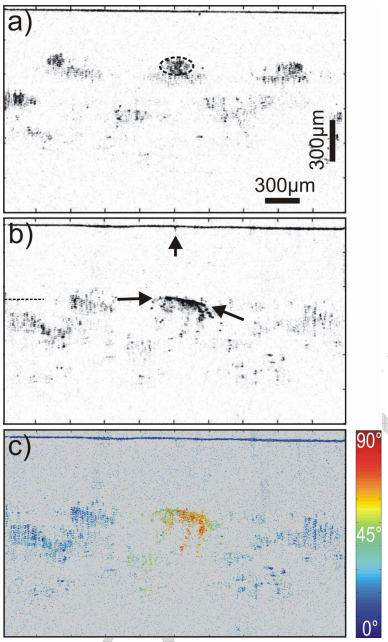

Figure 8 (two columns suggested):